07 Nov 2017

# Experimental Measurement Of Residual Stress And Distortion In Additively Manufactured Stainless Steel Components With Various Dimensions

M. Ghasri-Khouzani

H. Peng

R. Rogge

R. Attardo

*et. al. For a complete list of authors, see https://scholarsmine.mst.edu/mec_aereng_facwork/5188*



## Recommended Citation

M. Ghasri-Khouzani et al., "Experimental Measurement Of Residual Stress And Distortion In Additively Manufactured Stainless Steel Components With Various Dimensions," *Materials Science and Engineering: A*, vol. 707, pp. 689 - 700, Elsevier, Nov 2017.
The definitive version is available at https://doi.org/10.1016/j.msea.2017.09.108

Materials Science & Engineering A 707 (2017) 689–700

Contents lists available at ScienceDirect

Materials Science & Engineering A

journal homepage: www.elsevier.com/locate/msea

# Experimental measurement of residual stress and distortion in additively manufactured stainless steel components with various dimensions

M. Ghasri-Khouzani[a,*], H. Peng[b], R. Rogge[c], R. Attardo[d], P. Ostiguy[d], J. Neidig[e], R. Billo[f], D. Hoelzle[g], M.R. Shankar[a]

[a] Department of Industrial Engineering, University of Pittsburgh, Pittsburgh, PA 15261, United States
[b] Department of Aerospace and Mechanical Engineering, University of Notre Dame, Notre Dame, IN 46556, United States
[c] Canadian Neutron Beam Centre, Chalk River Laboratories, Chalk River, Canada ON K0J 1J0
[d] DePuy Synthes, Johnson & Johnson Company, Raynham, MA 02767, United States
[e] ITAMCO, Plymouth, IN 46563, United States
[f] Department of Computer Science and Engineering, University of Notre Dame, Notre Dame, IN 46556, United States
[g] Department of Mechanical and Aerospace Engineering, The Ohio State University, Columbus, OH 43210, United States

ARTICLE INFO

*Keywords:*
Additive manufacturing
Neutron diffraction
Stainless steel
Residual stress
Distortion

ABSTRACT

Disk-shaped 316L stainless steel parts with various diameters and heights were additively manufactured using a direct metal laser sintering (DMLS) technique. Neutron diffraction was used to profile the residual stresses in the samples before and after removal of the build plate and support structures. Moreover, distortion level of the parts before and after the removal was quantified using a coordinate measuring machine (CMM). Large tensile in-plane stresses (up to ≈ 400 MPa) were measured near the as-built disk top surfaces, where the stress magnitude decreased from the disk center to the edges. The stress gradient was steeper for the disks with smaller diameters and heights. Following the removal of the build plate and support structures, the magnitude of the in-plane residual stresses decreased dramatically (up to 330 MPa) whereas the axial stress magnitude did not change significantly. The stress relaxation caused the disks to distort, where the distortion metric was higher for the disks with smaller diameters and heights. The distribution of the residual stresses revealed a marked breakdown of self-similarity in their distribution even comparing disk-shaped samples that were fabricated under identical printing parameters; the stress field profiles were not linearly scaled as a function of height and diameter.

## 1. Introduction

Additive manufacturing (AM) has received considerable attention in recent years due to its ability to create complex near-net-shape geometries that are difficult to achieve using conventional manufacturing techniques. In contrast to machining processes where excess material is removed from a large workpiece to achieve the desired geometry, during AM, the near-net-shape part is fabricated in a layer-by-layer manner. Various AM techniques have been developed over the last three decades, and exhibited beneficial results [1–3]. AM offers a framework for transcending conventional constraints placed on designs due to the reliance on subtractive processes. For example, highly interdigitated, re-entrant shapes that are difficult to fabricate using traditional processes become realizable via AM. In metals-based AM, direct metal laser sintering (DMLS) is the most widespread process at present owing to its capability to build full dense components with mechanical properties insignificantly different from those exhibited by wrought parts. In this technique, a focused laser beam is used as a heat source to sinter or melt successive layers of metallic powder on top of one another [4,5]. Different metallic materials have been used in DMLS including nickel-based superalloys [6–8], steels [9–12], titanium alloys [13,14] and aluminum alloys [15,16]. However, the high temperature gradients imposed by DMLS limit the integrity and microstructural homogeneity of the resulting components. Each powder layer undergoes preheating, melting, rapid solidification, and partial remelting. The severe temperature gradients induce large residual stresses within the as-built parts, which can exceed the material yield strength in some cases. These stresses can lead to reduction in the strength of the component, and may favor propagation of micro-cracks. Moreover, residual stresses can cause significant distortion of the component after build plate removal [17].

Various techniques have been used for measuring residual stresses in additively manufactured components [9,11,17–34]. These techniques can be divided into destructive and non-destructive ones. One of

* Corresponding author.
*E-mail address:* mog20@pitt.edu (M. Ghasri-Khouzani).

http://dx.doi.org/10.1016/j.msea.2017.09.108
Received 23 July 2017; Received in revised form 22 September 2017; Accepted 23 September 2017
Available online 24 September 2017
0921-5093/ 

**Table 1**
Catalog of printed disk artifacts. Y and N denote "Yes" and "No", respectively.

| Case Number | 1 | 2 | 3 | 4 | 5 | 6 | 7 | 8 | 9 | 10 | 11 | 12 | 13 | 14 |
|---|---|---|---|---|---|---|---|---|---|---|---|---|---|---|
| Diameter (mm) | 25 | 35 | 45 | 55 | 65 | 70 | 75 | 80 | 45 | 45 | 45 | 45 | 45 | 45 |
| Height (mm) | 5 | 5 | 5 | 5 | 5 | 5 | 5 | 5 | 1 | 3 | 10 | 15 | 20 | 30 |
| Stress Measurement | N | N | Y | N | N | Y | N | Y | N | N | Y | Y | N | N |
| Distortion Measurement | Y | Y | Y | Y | Y | Y | Y | Y | Y | Y | Y | Y | Y | Y |

the destructive techniques is hole-drilling [19,21,22,35], in which a specific amount of material is removed by drilling, and the resulting deformation (or strain) is measured to calculate the stress. A more recent destructive technique is the contour method [24–27,30,33,36] which involves three steps: specimen cutting by electric discharge machining (EDM), measuring contours of both cut surfaces using coordinate measuring machine (CMM), and calculating stresses using finite element modeling. Crack compliance method [17,37] is another destructive technique, which utilizes metallic foil strain gauges to measure the strain released during successive extension of a slot into the depth of the part. The main drawback of these techniques is their destructive nature that does not allow for sequential measurements of residual stress in the same part after multiple processes such as build plate removal or heat treatments. The most widely used non-destructive techniques for residual stress measurements revolve around Bragg's law of diffraction, which can be used to measure the lattice interplanar spacing, $d_{hkl}$, in the stressed and stress-free specimens. The elastic strain is calculated from the change in $d_{hkl}$ due to tensile or compressive stress within the material. X-ray diffraction (XRD) technique [9,17,23,34] is limited to near-surface stress measurements due to relatively low penetration depth of X-ray beams ($\approx$ 5 μm for steels). However, neutron diffraction [11,18–20,25–29,31–33] has commonly been applied for measuring volumetric residual stresses owing to deep penetration of neutrons into metals ($\approx$ 50 mm for steels). More recently, high energy ($>$ 80 keV) synchrotron X-ray sources have provided the capability to measure stresses at depth. However, due to the short wavelengths ($\approx$ 0.1 Å) associated with high energy X-rays, their diffraction angles are relatively low (2–20°) leading to an elongated prism shape for the sampled gauge volume [38]. Thus, it is difficult to measure strain along three principal directions at each point without any extrapolations. By contrast, the diffraction angle for neutron technique is usually 90° resulting in a cuboidal sampled gauge volume, which makes it feasible to measure all strain components at each point of interest [39].

Several residual stress and distortion studies have been conducted on additively manufactured stainless steels [9,11,17,23,27,31,33,34]. Rangaswamy et al. [27] profiled residual stresses in 316 L stainless steel thin walls and pillars with rectangular and square cross-sections, respectively. They found negligible in-plane stresses but significant compressive axial stresses at most locations [27]. Wu et al. [33] investigated the effect of AM process parameters on residual stresses in prism and L-shaped components. They found significant tensile in-plane stresses near the top surface of the components, and concluded that this causes the parts to distort after build plate removal. Moreover, their observations revealed that in-plane residual stresses are influenced by scan pattern whereas axial residual stresses remain unaffected [33]. In a more recent study, Brown et al. [11] mapped residual stresses in GP-1 stainless steel parts having a Charpy test sample geometry. They reported that presence of a notch in the part geometry caused an asymmetry stress state, which remained after removal of build plate and support structures [11].

The objective of the present contribution is to examine the influence of component dimensions on residual stress and distortion distribution. Several 316 L stainless steel components with the same geometry (disk) but different dimensions (diameters of 25–80 mm and heights of 1–30 mm) were fabricated by DMLS with the same process parameters. The disk geometry simplified quantification of distortion level. Change in the disk diameter and height (number of powder layers) was expected to affect the temperature distribution within the part, and consequently the residual stresses and distortion level. Neutron diffraction was used to map residual stresses within the components both before and after build plate removal of base plate and support structures. Furthermore, a coordinate measuring machine (CMM) was used to quantify distortion level of the parts before and after the removal.

## 2. Experimental procedure

### 2.1. Artifacts

Disk artifacts were printed with different diameters and heights, as listed in Table 1. One sample was printed for each case. All 14 samples were built on top of Materialise Magics block style support structures. The location of the support structure with respect to an individual sample and base plate as well as the support structure parameters is schematically illustrated in Fig. 1. The support structure parameters were the same for all samples and are listed in Table 2. The support structures were used to facilitate the removal of samples from the build plate and also reduce distortion arising from thermal stresses. After measurements of residual stress and distortion on the as-built samples, they were removed from the base plate and support structures using a cut off wheel and an EDM wire, respectively.

### 2.2. Feedstock powder and AM technique

A prealloyed gas atomized 316L stainless steel powder was used as the feedstock material in this study. The chemical composition of the powder is shown in Table 3. All disk-shaped specimens were built through DMLS technique using an EOS M290 machine. A powder layer thickness of 20 μm was employed with an Yb-fiber laser power of

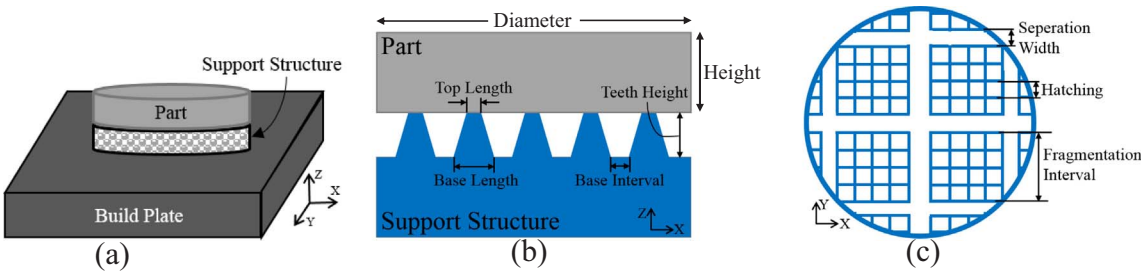


**Fig. 1.** (a) Schematic of support structure location with respect to an individual sample and base plate. (b) and (c) Schematic of support structure parameters.

**Table 2**
Support structure parameters (mm).

| Total height | Fragmentation | Hatching | Teeth height | Teeth base interval | Teeth base length | Teeth top length |
|---|---|---|---|---|---|---|
| 5 | X-interval = 4 Y = 0.8 separation width = 0.2 | X = 0.8 Y = 0.8 | 0.5 | 0 | 0.5 | 0.2 |

**Table 3**
Chemical composition of 316L stainless steel powder used as the feedstock material (wt %).

| C | Cr | Mn | Mo | N | Ni | O | S | Si | Fe |
|---|---|---|---|---|---|---|---|---|---|
| 0.03 | 17.9 | 2.0 | 2.4 | 0.1 | 13.9 | 0.04 | 0.01 | 0.75 | Balance |

195 W and a scan speed of 1083 mm/s. An alternating scan pattern was applied, where the hatching direction was rotated by 67° between the consecutive layers. An ultra-high purity argon gas was purged into the chamber during printing to keep the oxygen content less than 0.1%. To reduce stresses imposed by thermal cycles, the build plate temperature was maintained at 80 °C. The build plate was a hot rolled mild steel panel with dimensions of 252 mm × 252 mm × 18 mm.

### 2.3. Residual stress measurements

Neutron diffraction residual stress measurements were performed on the L3 diffractometer of the Canadian Neutron Beam Center, located in the NRU reactor, at Canadian Nuclear Laboratories. Neutrons with wavelength of 1.508 Å diffracted from the {511} planes of a germanium monochromator were employed. The incident beam cross-section was set using 2 mm × 2 mm apertures. Neutron diffraction provides the capability to non-destructively measure residual stresses within bulk of many engineering materials. The technique uses Bragg's law for yielding residual elastic strains along principal directions, from which the corresponding residual stresses can be computed. The elastic lattice strain in the sampled gauge volume for a specific {*hkl*} planes can be calculated using [39]:

$$\varepsilon_{hkl} = \frac{d_{hkl} - d_{0,hkl}}{d_{0,hkl}} \quad (1)$$

where $d_{hkl}$ and $d_{0,hkl}$ are lattice interplanar spacing for the sample under study, and a stress-free reference sample, respectively. There are several methods to determine a stress-free reference [40]. A common method is to cut small cubes or matchsticks from the sample under investigation or a duplicate. In the present contribution, two coupons with dimensions of 20 mm × 2 mm × 2.5 mm were cut from a sister sample along the length and width direction by EDM. To ensure that the extracted coupons were stress-free, another pair of them was annealed under argon atmosphere at 900 °C for 1 h, followed by furnace cooling. The values of $d_{hkl,0}$ for these four coupons were insignificantly (less than 3%) different, indicating that even the non-heat treated coupons were strain-free. Thus, their average was taken for lattice strain calculations in this study. The principal stresses (e.g. $\sigma_{xx}$, $\sigma_{yy}$, and $\sigma_{zz}$) can be calculated from measured lattice strains (e.g. $\varepsilon_{xx}$, $\varepsilon_{yy}$, and $\varepsilon_{zz}$) using Hook's law:

$$\sigma_{ii} = \frac{E_{hkl}}{(1+\nu_{hkl})(1-2\nu_{hkl})}[(1-\nu_{hkl})\varepsilon_{ii} + \nu_{hkl}(\varepsilon_{jj} + \varepsilon_{kk})] \quad (2)$$

where $E_{hkl}$ and $\nu_{hkl}$ are {*hkl*} diffraction peak specific elastic modulus and Poisson ratio, respectively.

Based on length scale, residual stresses can be categorized into two types: Type I stresses, or macro-scale stresses, which change over large distances comparable to the dimensions of the work-piece, and Type II stresses, or micro-scale stresses, which change over the order of grains. Type II stresses, or intergranular stresses, originate from anisotropy in different crystallographic orientations at the grains. Thus, it is of importance for macroscopic residual stress measurements to choose an {*hkl*} diffraction peak with minimum contribution from Type II stresses [27,38]. In the case of austenitic stainless steel, {311} diffraction peak has shown to have little sensitivity to intergranular stresses [41]. Thus, this diffraction peak was used for residual stress measurements in this contribution. The elastic constants for the {311} planes, $E_{311}$ and $\nu_{311}$, were taken to be 184 GPa and 0.294, respectively [27].

The residual stresses within the additively manufactured samples were measured before and after removal of both build plate and support. For each sample, measurements were performed at a series of locations along longitudinal (x) and transverse (y) directions at three different heights, as schematically illustrated in Fig. 2. In this way, the disk center points (X = Y = 0) were measured two times. For the other locations, however, one measurement at each point was performed. The uncertainty in the residual strain measurements was estimated based on fitting the diffraction peaks by symmetrical Gaussian profiles. Each location was measured in three different orientations to allow the calculation of the stress along three principal directions.

### 2.4. Distortion measurements

The geometrical characteristics of the printed samples were measured using a coordinate measuring machine (CMM), Renishaw Cyclone Series 2, before and after removal of both build plate and support structures. The machine had a 1-μm position resolution with axial repeatability of ± 2 μm within its full travel area. In all cases, contact scanning was carried out using a Renishaw's SP620 touch trigger probe with a 3-mm tip diameter and a length of 140 mm. For each sample, three measurements were performed with different datum locations. Renishaw's Tracecut 24a software was used for point cloud data acquisition. Fig. 3 presents typical point clouds for top surface of a disk with diameter of 45 mm and height of 5 mm before and after removal of

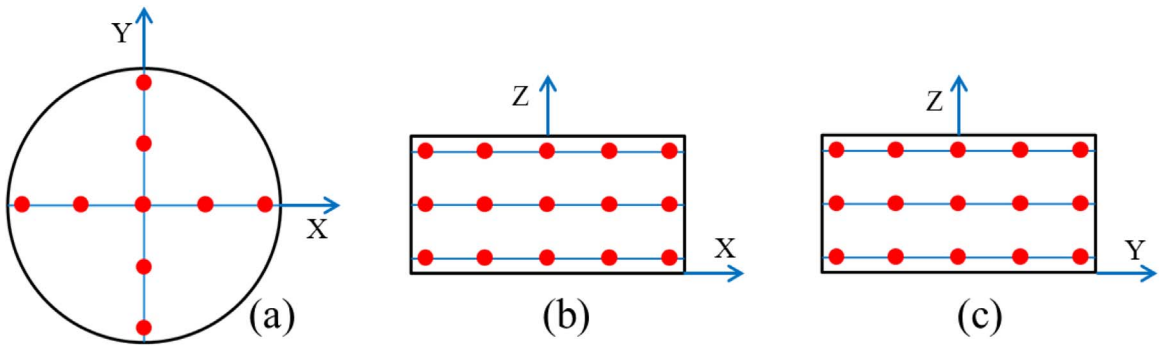


**Fig. 2.** Schematic illustration of measurement point locations; (a) horizontal section (top view), (b) vertical section (front view), and (c) vertical section (side view).

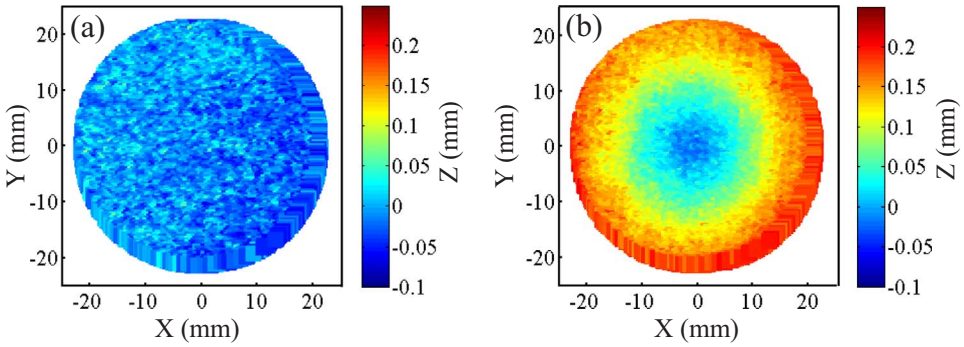


**Fig. 3.** Coordinate point clouds for top surface of a disk with diameter and height of 45 mm and 5 mm, respectively before (a) and after (b) removal of the build plate and support structures.

the build plate and support structures. The point clouds after removal had a half-sphere geometry. Thus, the distortion level was defined by a single metric, the radius of curvature of a sphere fit to the point cloud. A search algorithm

$$\min_{x_c,y_c,z_c,r} J \tag{3}$$

was applied to minimize an objective function, $J$, which was defined as the square of the distance between point-cloud data points, $(x_i, y_i, z_i)$, and a sphere centered at $(x_c, y_c, z_c)$ with radius $r$:

$$J = \sum [(x_i - x_c)^2 + (y_i - y_c)^2 + (z_i - z_c)^2 - r^2]^2. \tag{4}$$

Radius $r$ was taken as the radius of curvature (ROC) for each disk. The higher the ROC value, the lower the distortion level.

## 3. Results

### 3.1. Residual stresses before removal of build plate and support structures

Fig. 4 depicts the three residual stress components ($\sigma_{xx}$, $\sigma_{yy}$, and $\sigma_{zz}$) for a disk with a height of 5 mm and diameter of 80 mm as a function of position along x and y directions. The stress changes along x and y direction were relatively similar, though some inconsistencies were observed close to edges. The similarity of the stress profiles was attributed to the symmetric sample geometry as well as the applied scan pattern during DMLS, where the scan direction was rotated by 67° between consecutive layers. For the remaining experimental samples, the stress profiles along one direction (either x or y) will be presented to avoid repetition. From Fig. 4, it can also be seen that the x and y stress components ($\sigma_{xx}$ and $\sigma_{yy}$) profiles were similar to each other with changing from tension near the top surface to compression near the bottom surface for all measurement locations along both x and y directions. The bending moment was asymmetric, where most stress-free points were shifted from the sample mid-height (Z = 2.5 mm) towards its bottom surface due to constraint from the build plate and support structures. The z component stresses ($\sigma_{zz}$), however, were close to zero in all locations.

Further inspection of Fig. 4 reveals that at both 2.5 mm and 3.75 mm heights from the bottom surface, the tensile in-plane stress ($\sigma_{xx}$ and $\sigma_{yy}$) magnitude decreased dramatically from the center (X = Y = 0 mm) to the edges (X = ± 35 mm or Y = ± 35 mm) along both x and y directions. This change was so sharp in some cases that the stresses became compressive near the sample edges. The largest tensile

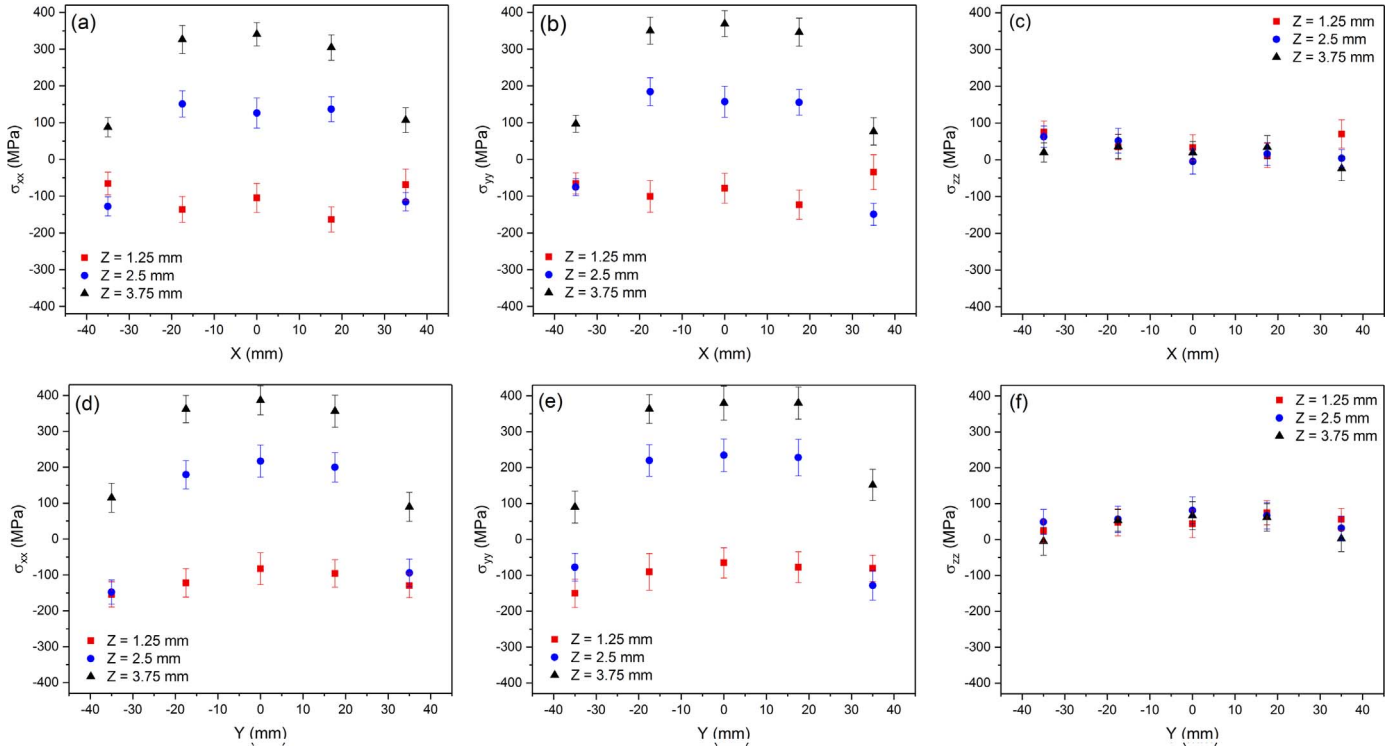


**Fig. 4.** Stress profiles along x (a-c) and y (d-f) directions at different heights for a disk with diameter and height of 80 mm and 5 mm, respectively, while still attached to support structures and build plate.

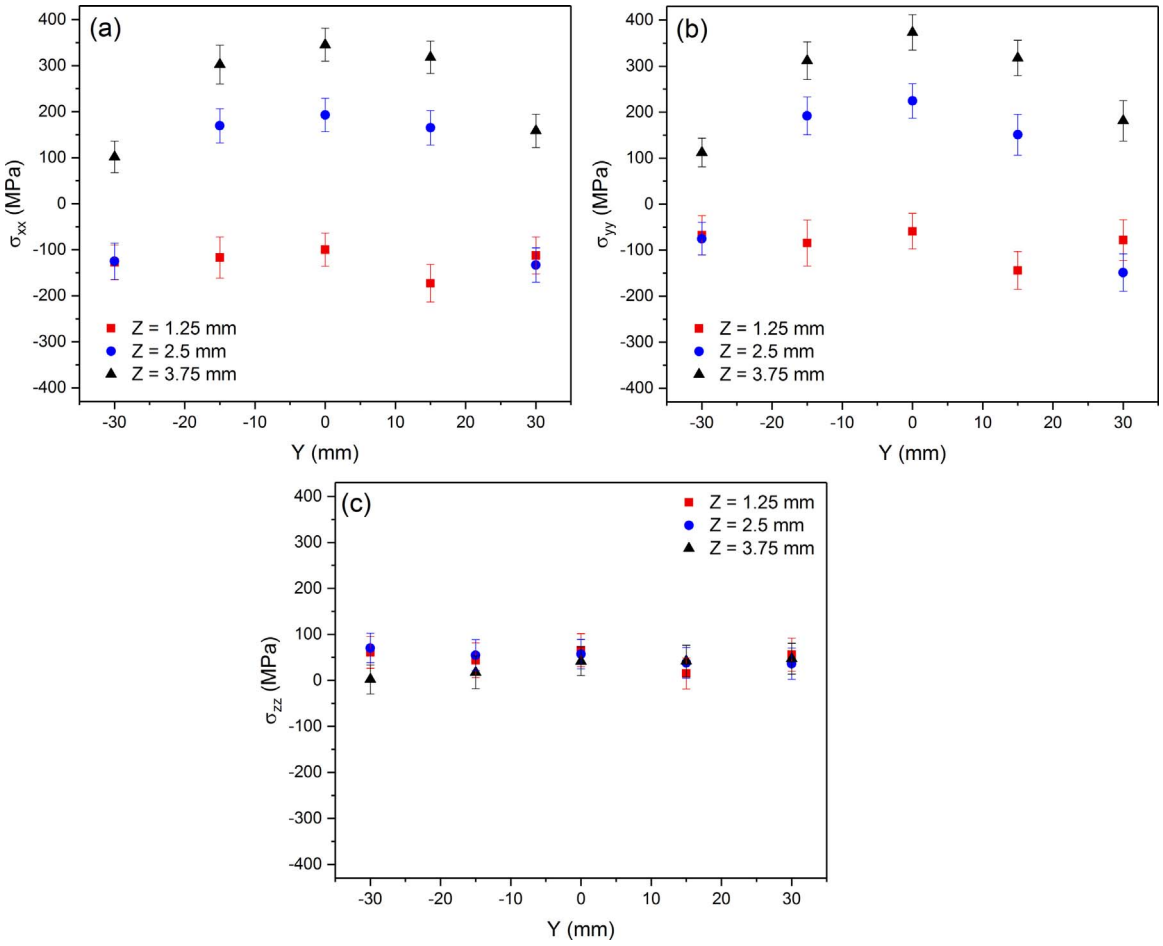


**Fig. 5.** X, Y, and Z components of stress as a function of position along y direction in a disk with diameter and height of 70 mm and 5 mm, respectively before removal from build plate and support structures.

stress was observed near the top surface (Z = 3.75 mm) at the disk center with an average value of 369 ± 35 MPa.

The stress profiles along y direction for a disk with a diameter of 70 mm and height of 5 mm are shown in Fig. 5. Both in-plane and axial stress profiles were similar those observed for the 80 mm diameter disk (Fig. 4) with a bending moment of in-plane stresses and negligible axial ones.

Fig. 6 shows the X, Y, and Z components of the residual stresses profiled along y direction in a sample with diameter and height of 45 mm and 5 mm, respectively. Near the top surface of the disk (Z = 3.75 mm), large tensile in-plane stresses (≈ 350 MPa) were present at the center (Y = 0 mm) and symmetrically approached zero at the edges (Y = ± 18 mm). At the mid-height of the disk (Z = 2.5 mm), the in-plane stresses changed from tension (≈ 230 MPa) at the center to compression (roughly −200 MPa) at the edges. Near the bottom surface of the disk (Z = 1.25 mm), an approximate parabolic distribution of compressive in-plane stresses were observed. The magnitude of the compressive stress was approximately 190 MPa and 0 MPa at the center and edges, respectively. In the case of the axial stresses, the residual stress magnitude in all locations was negligible. Comparison of Fig. 6 with Figs. 4 and 5 reveals that the in-plane residual stress gradient of the 45 mm-diameter disk was three times steeper than that of the 70 mm and 80 mm diameter ones. This can be attributed to the cooling rate difference between the part center and edges, where the difference for 45 mm diameter disk is significantly greater than that of the 70 mm and 80 mm diameter ones.

Residual stress profiles of a disk with a diameter of 45 mm and height of 10 mm are provided as a function of position in Fig. 7. Tensile in-plane stresses were observed near the top and bottom surfaces of the disk, whereas compressive in-plane stresses were present at mid-height of the sample (Z = 5 mm). Based on this residual stress distribution, there seemed to be two neural manifolds at the sample; one above of the mid-height and another below it. To ensure about this, two extra points were measured at the disk center (X = Y = 0 mm) and heights of Z = 3 mm and Z = 7 mm, as shown in Fig. 7. The in-plane stresses at these two points were close to zero, confirming presence of two neutral manifolds. This trend was dramatically different from the one observed for the 5 mm-height disks (Figs. 4–6), where the in-plane stresses changed from tension near the disk top surface to compression near the bottom surface and formed a bending moment with a single neutral manifold. The breakdown of the profile of the stress field through the height as a function of the geometry is noteworthy. The doubling of the height of the sample does not result in simple scaling the profile of the stress-field. Instead, a non-linear variation emerges.

Further inspection of Fig. 7 shows that the magnitude of the tensile in-plane stresses near the disk top surface (Z = 8.75 mm) oscillated around 300 MPa along y direction. Near the bottom surface of the disk (Z = 1.25 mm), however, the in-plane stress magnitude increased from ≈ 100 MPa at the center (X = Y = 0 mm) to ≈ 220 MPa at the edges (Y = ± 18 mm). The magnitude of the compressive in-plane stresses at mid-height of the disk (Z = 8.75 mm) was roughly 200 MPa at all locations along x axis. Z component residual stresses were around zero in all measurement locations of the sample, similar to the trend observed for the 5 mm-height disks (Figs. 4–6).

Fig. 8 depicts the three residual stress components ($\sigma_{xx}$, $\sigma_{yy}$, and $\sigma_{zz}$) for a disk with a height of 15 mm and diameter of 45 mm as a function

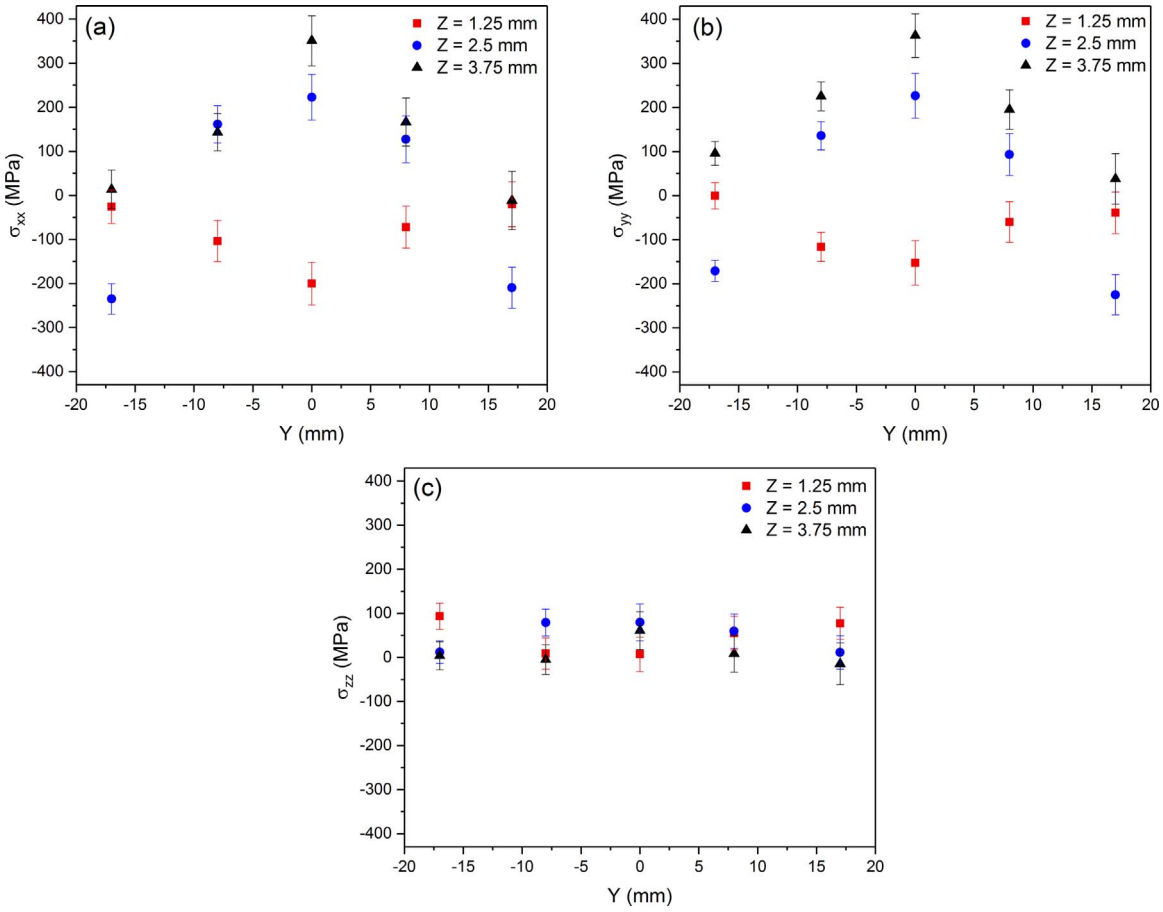


**Fig. 6.** Residual stresses along y direction for a disk with diameter and height of 45 mm and 5 mm, respectively, while still attached to support structures and build plate.

of position along x direction. Near the bottom and top surfaces of the disk (Z = 1.25 mm and Z = 13.75 mm), large tensile in-plane stresses (≈ 350 MPa) were present at all locations along x direction. At the mid-height of the disk (Z = 7.5 mm), however, compressive in-plane stresses were observed, whose magnitude decreased from ≈ 200 MPa at the center (X = 0) to ≈ 0 MPa at the edges (Y = ± 18 mm). From the distribution of the in-planes residual stresses, two neutral manifolds seemed to be present in this sample, similar to what observed for the 10 mm-height disk in Fig. 7.

From Fig. 8(c), it can be seen that the axial residual stresses were around 0 MPa and 100 MPa near the bottom and top surfaces of the disk, respectively. At the mid-height of the disk, the magnitude of the tensile axial stresses rose from ≈ 50 MPa at the center (X = 0) to ≈ 100 MPa at the edges (Y = ± 18 mm).

### 3.2. Residual stresses after removal of build plate and support structures

Fig. 9 shows the residual stress profiles for the disk with height of 5 mm and diameter of 70 mm after parting from the build plate and support structures. The stress changes along x and y direction were relatively similar, though some inconsistencies were observed close to edges. This indicates that the residual stress distribution remained symmetric after removal of the base plate and support structures. For the remaining experimental samples, the stress profiles along one direction (either x or y) will be presented to avoid repetition. From Fig. 9, it can also be seen that the x and y stress components ($\sigma_{xx}$ and $\sigma_{yy}$) profiles were insignificantly different from each other.

Further inspection of Fig. 9 reveals that at both 2.5 mm and 3.75 mm heights from the disk bottom surface, the in-plane residual stresses ($\sigma_{xx}$ and $\sigma_{yy}$) altered from tension at the center (X = Y = 0 mm) to compression at the edges (X = ± 30 mm or Y = ± 30 mm) along both x and y directions. However, the stress gradient at disk mid-thickness (Z = 2.5 mm) was steeper than near the top surface (Z = 3.75 mm). Near the disk bottom surface (Z = 1.25 mm), the in-plane residual stresses were around 50 MPa in all locations. Comparison of Fig. 9 with Fig. 5 will show that the magnitude of the in-plane residual stresses in most locations decreased dramatically (up to 300 MPa) following the removal of the build plate and support structures. However, the stress relaxation at the disk edges was less significant compared to the center. The axial residual stresses did not change significantly after the base plate and support structure removal.

Residual stress profiles of the disk with diameter of 45 mm and height of 5 mm as a function of position after removal of the build plate and support structures are provided in Fig. 10. Near the top surface (Z = 3.75 mm) and mid-height (Z = 2.5 mm) of the disk, the in-plane stresses changed from tension at the center (Y = 0) to compression at the edges (Y = ± 18 mm). However, the stress gradient near the disk top surface was more stabilized than that at the mid-height. The in-plane residual stresses in all locations near the disk bottom surface (Z = 1.25 mm) were tension with a magnitude oscillating around 80 MPa. In the case of the axial residual stresses (Fig. 10(c)), tensile stress magnitude increased from zero near the top surface to ≈ 150 MPa near the bottom surface. Comparison of Figs. 6 and 10 reveals that the removal of the build plate and support structures resulted in a dramatic in-plane stress relaxation (up to 330 MPa). However, the stress relaxation was not identical for all locations along y direction with being more significant at the disk center compared to the edges. The removal of the build plate and support structures also led to an increase (≈ 100 MPa) in the magnitude of the axial stresses near the disk bottom surface.

Fig. 11 depicts the three residual stress components ($\sigma_{xx}$, $\sigma_{yy}$, and $\sigma_{zz}$) for the disk with height of 10 mm and diameter of 45 mm as a function of position along y direction following the removal of the base

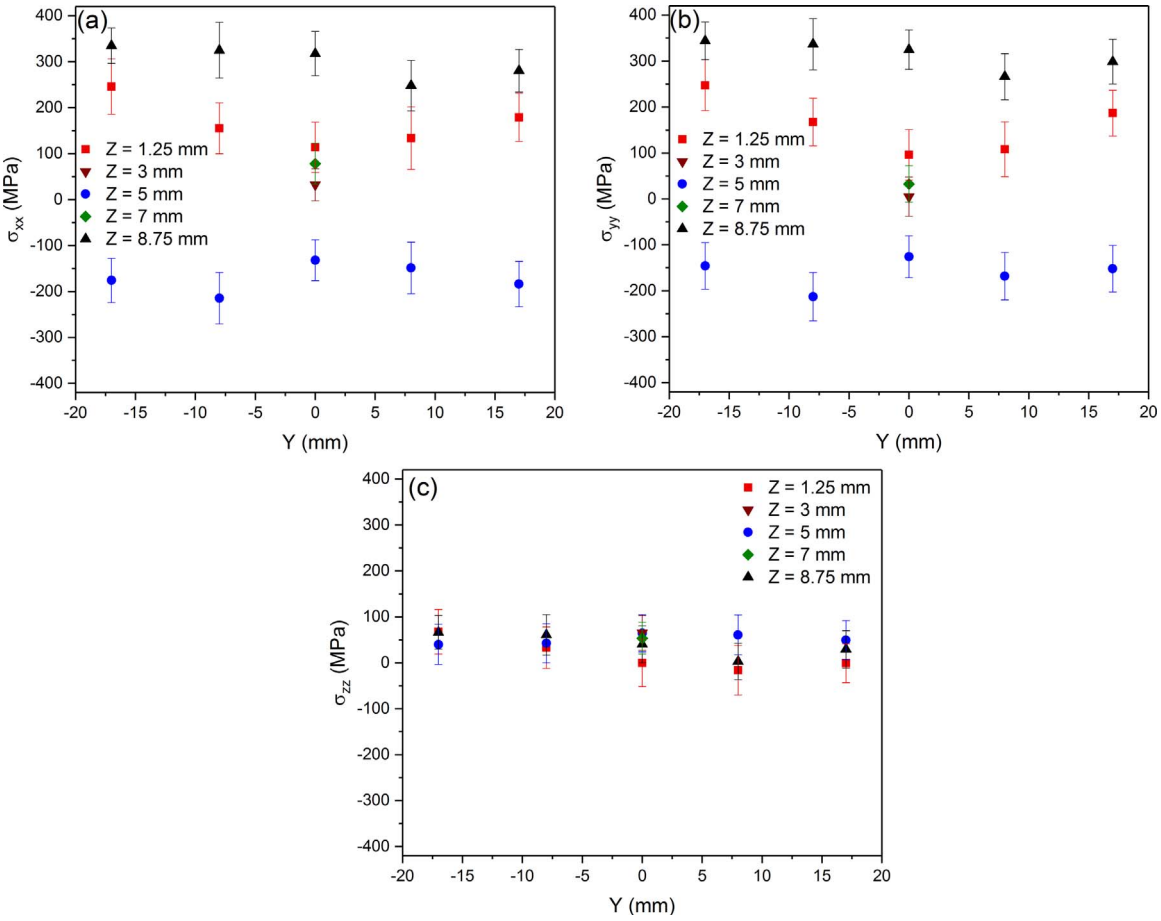


**Fig. 7.** Stress profiles along y direction at different heights for a disk with diameter and height of 45 mm and 10 mm, respectively before removal from build plate and support structures.

plate and support structures. To avoid confusion, the data are also listed in Table 4. The in-plane residual stresses were tensile near the top and bottom surfaces of the disk, and compressive at mid-height of the sample. Based on this residual stress distribution, it can be found that there were two neutral manifolds at the disk, similar to that observed before the removal of the build plate and support structures (Fig. 7). However, the removal led to a significant decrease in the magnitude of in-plane stresses near the disk top surface. It also stabilized the in-plane stress gradient near the disk bottom surface. Nevertheless, the in-plane residual stresses at the disk mid-height remained unchanged after the removal. In the case of the axial residual stresses, the stress magnitude at Z = 1.25, 3 and 5 mm and $-8 < Y < 8$ increased following the removal.

### 3.3. Distortion analysis

CMM was performed on the DMLS fabricated parts before and after removal of the build plate and support structures to quantify the distortion level. When the parts were attached to the base plate and support structures, their top surface was almost flat (Fig. 3(a)), and it was not possible to fit a sphere to their point clouds. Removal of the base plate and support structures, however, caused significant distortion in most parts, as representatively shown for the disk with the diameter of 45 mm and height of 5 mm in Fig. 3(b). Thus, the parts point clouds were fitted by a sphere to obtain the radius of curvature (ROC). Fig. 12 presents the ROC values for the disks with various dimensions. The distortion level of the disks decreased significantly (ROC increased) when their diameter or height became larger. This can be explained by the observed residual stress profiles before removal of the build plate and support structures, where the in-plane stress gradient from the disk center to the edges was steeper for the disks with smaller diameter or heights. This is in agreement with findings of Wu et al. [33] for additively manufactured 316 L stainless steel parts with prism geometry. The higher distortion level of 5 mm height disk than that of the 10 mm height one (Fig. 12(b)) can also be attributed to the more significant stress relaxation observed for the former one.

Further inspection of Fig. 12 reveals that the ROC-height plot had a greater slope than the ROC-diameter one, and saturated when the disk height approached 15 mm. The ROC-diameter plot (Fig. 12(a)) is also expected to saturate when the ROC reaches 3000 mm, meaning the disks are almost flat.

## 4. Discussion

### 4.1. Explanation of the observed residual stress distributions

Residual stresses and distortion in the DMLS fabricated disk-shaped components were measured via neutron diffraction and CMM, respectively. When the disks were attached to the support structures and build plate, the maximum measured stress magnitude was roughly 400 MPa, close to the material yield stress (456 ± 17 MPa [42]), which is similar to that reported for rectangular plates [27], Charpy test specimens [11], cuboid [17], prism and L-shaped parts [33]. Thus, it can be concluded that the maximum residual stresses within the AM fabricated components is close to the feedstock materials yield point regardless of the component geometry and dimensions. It should be noted that the measurement points were ≈ 1.25 mm far from the sample top and bottom surfaces. Thus, it is likely that the in-plane stresses reach the yield point at these free surfaces. The distribution of the residual stresses seems to be highly dependent on the part dimensions. For the 5-

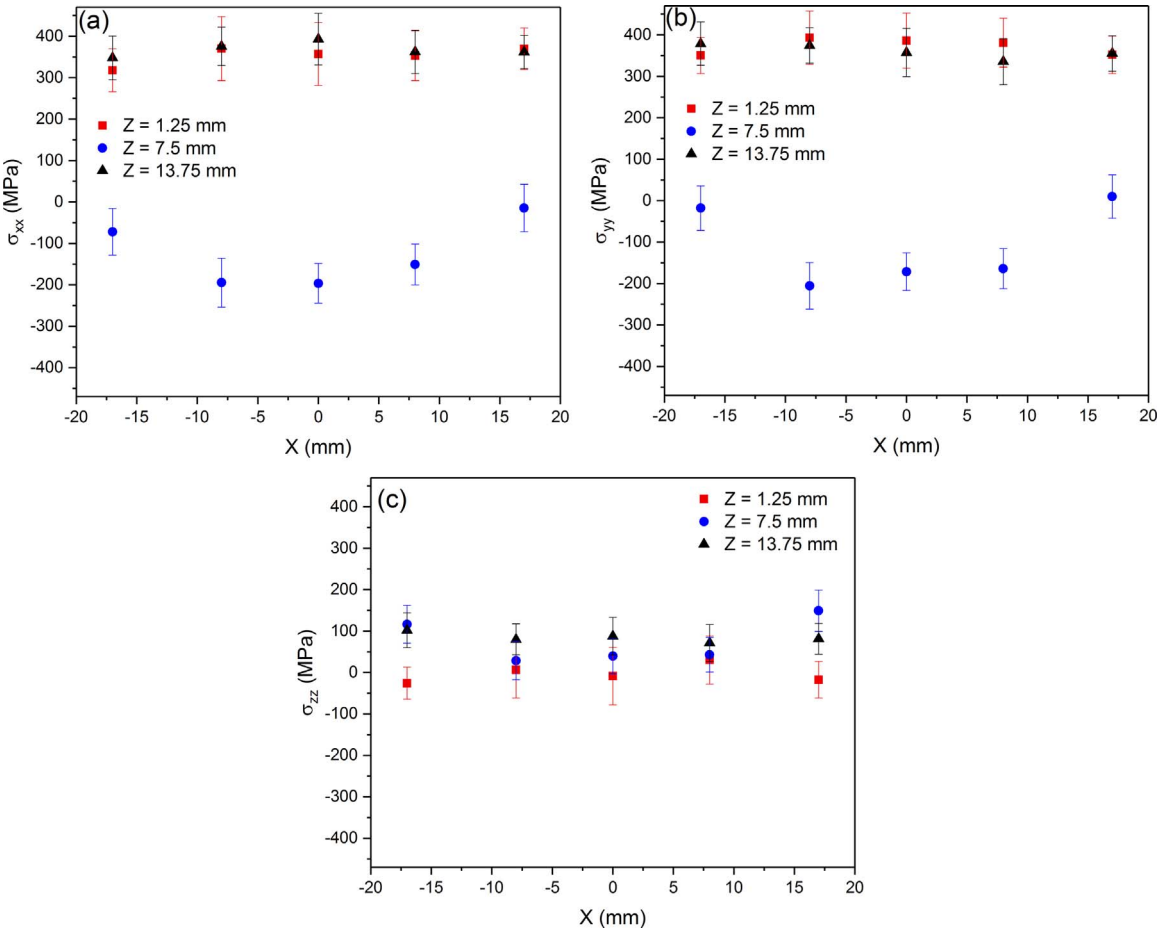


**Fig. 8.** X, Y, and Z components of stress as a function of position along x direction in a disk with diameter and height of 45 mm and 15 mm, while still attached to support structures and build plate.

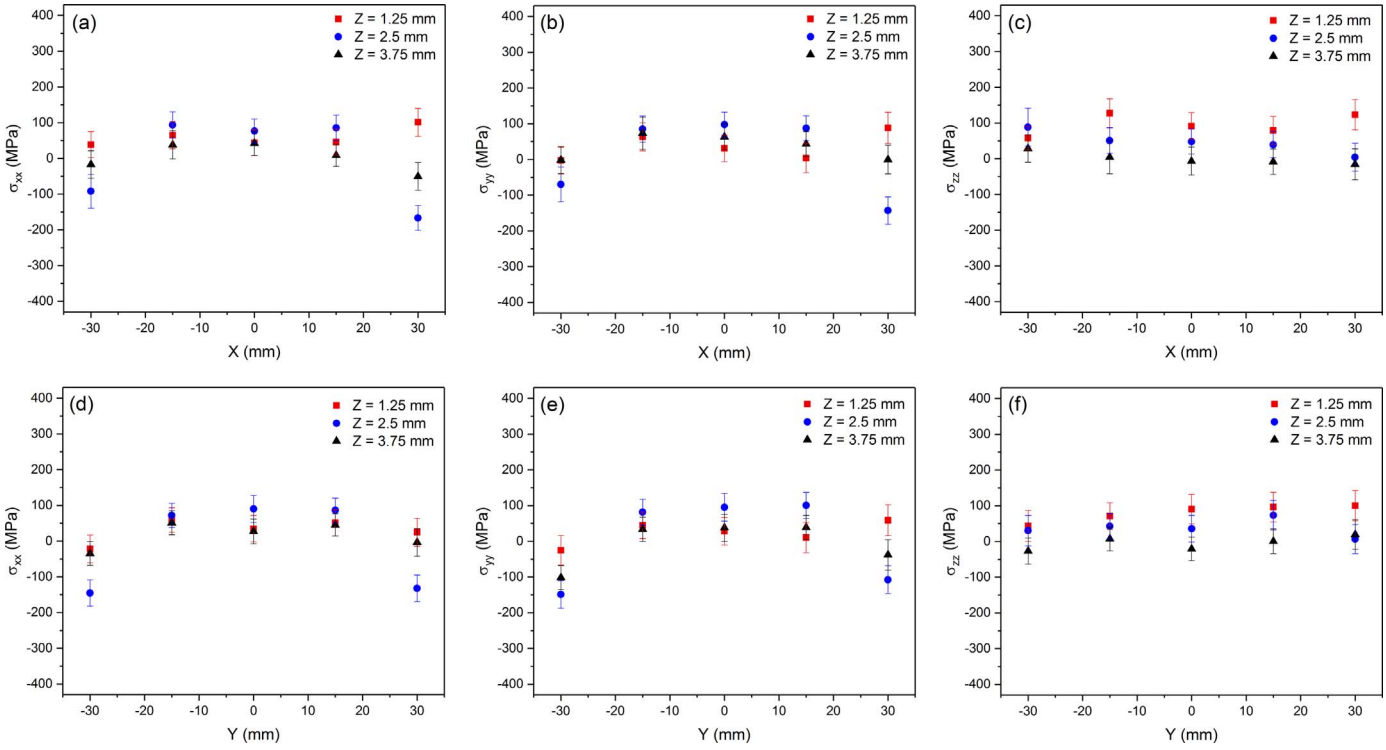


**Fig. 9.** Stress profiles along x (a-c) and y (d-f) directions at different heights for a disk with diameter and height of 70 mm and 5 mm, respectively after removal from the support structures and build plate.

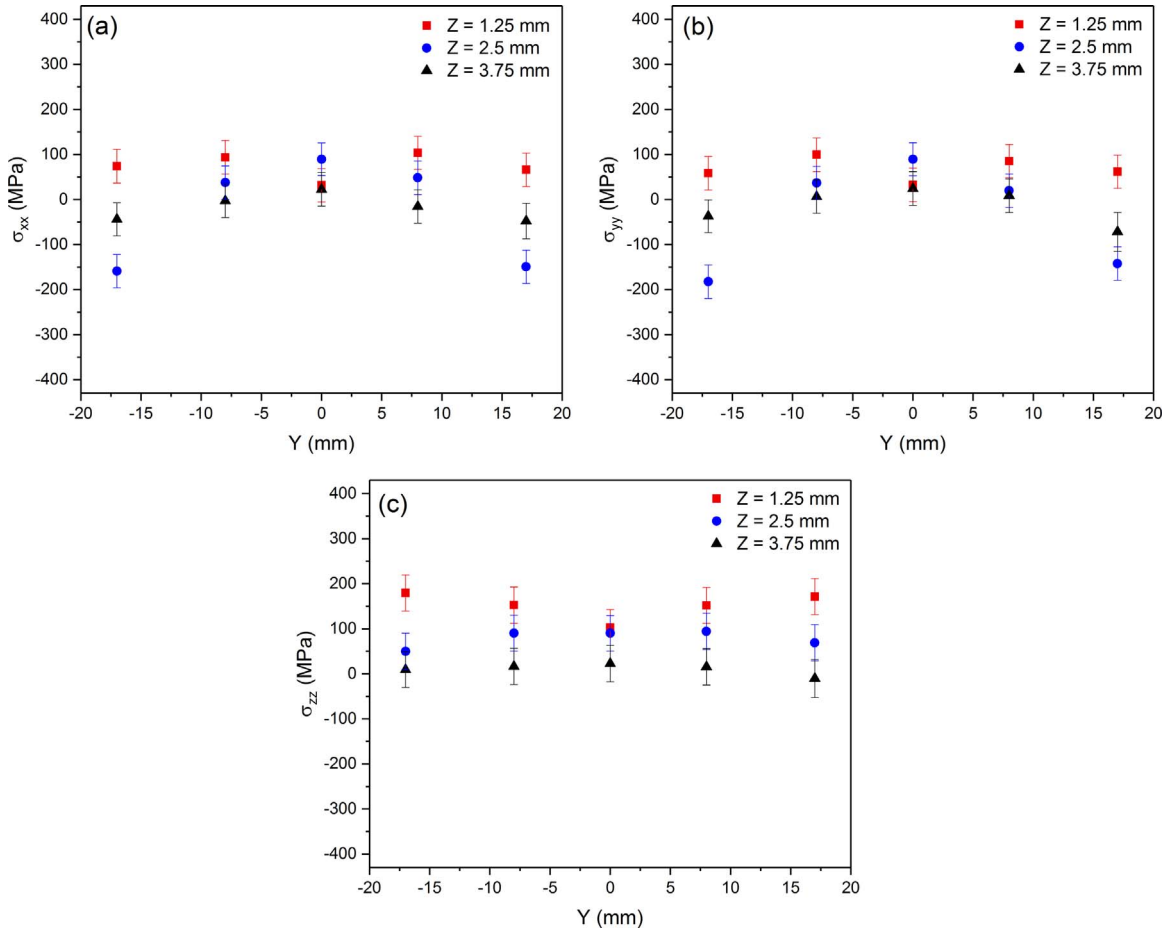


**Fig. 10.** Residual stresses along y direction for a disk with diameter and height of 45 mm and 5 mm, respectively after removal of the build plate and support structures.

mm height disks in this study, the in-plane residual stresses changed from tension near the top surface of the disks to compression near the bottom surface of the disks before removal of the build plate and support structures. The bending moment, which was also observed in the DMLS fabricated Charpy test specimens [11], can be explained in terms of localized thermal contraction during the DMLS process. When molten metal is deposited on a cold build plate in early stages of DMLS, it tries to shrink during solidification. However, this thermal contraction is constrained by the cold, rigid build plate, leading to creation of tensile in-plane stresses in the early deposited layers and compressive ones in the build plate. When a significant number of layers are deposited, the early layers are annealed and their tensile residual stresses are relieved. However, the solidification of newly added layers creates compressive in-plane stresses in both the build plate and early deposited layers (near the disk bottom surface). The last deposited layers (near the disk top surface) exhibit the greatest tensile in-plane stresses because they do not experience significant annealing whereas their contraction is constrained by a thick, cold metal.

In the case of the 10 mm and 15 mm height disks, the in-plane residual stresses were tension near both the top and bottom surfaces of the parts and compression at the mid-height. This residual stress profile is in agreement with that observed for a SLM fabricated 316 L stainless steel cuboid with a height of 10 mm [17]. It is believed that the part height (number of powder layers) is one of the most important parameters determining the magnitude and distribution of the residual stresses [17,19]. For instance, it was reported that the magnitude of tensile in-plane residual stresses increased by four times when the part height rose from 5 mm to 10 mm [17]. For tall components, the thermal contraction of the last deposit layers is mainly constrained by the component rather than the build plate. In the case of 5 mm height disks, the contraction was constrained by the bottom zone of the disk (5 mm far from the disk top surface). In the case of 10 mm height disks, 5 mm far from the disk top surface corresponds to the mid-height. Thus, the thermal contraction of the upper zone of the disk is constrained by the mid-height zone, resulting in creation of tensile residual stresses near the top surface and compressive one at the mid-height. Presence of tensile in-plane residual stresses near the bottom surface of 10 and 15 mm height disks seems to be attributed to the increased disk height, where their magnitude increased from roughly 150 MPa for the 10 mm height disk to approximately 350 MPa the 15 mm height one. Based on the observed dramatic change in the residual stress magnitude and distribution with the number of powder layers in this contribution and other studies [17,19], it seems that the stress states of the deposited layers evolve several times during the DMLS process. Thus, in-situ measurement of the residual stresses during the layer deposition should the subject of future study.

### 4.2. Correlation between the residual stresses and distortions

When the 5 mm height disks were attached to the build plate and support structures, the magnitude of the in-plane tensile stresses near the disk top surface (Z = 3.75 mm) and mid-height (Z = 2.5 mm) decreased significantly from the sample center (X = Y = 0) to the edges. The residual stress gradient was so sharp in some cases that the stress state changed from tension at the center to compression at the edges. This stress gradient which is also observed in the case of quenching [43] and welding [44] can be explained by temperature distribution within the component, where edges are colder and cool faster compared to the center [45]. The in-plane stress gradient can cause component distortion in both AM [11,19,22,25,29,33] and

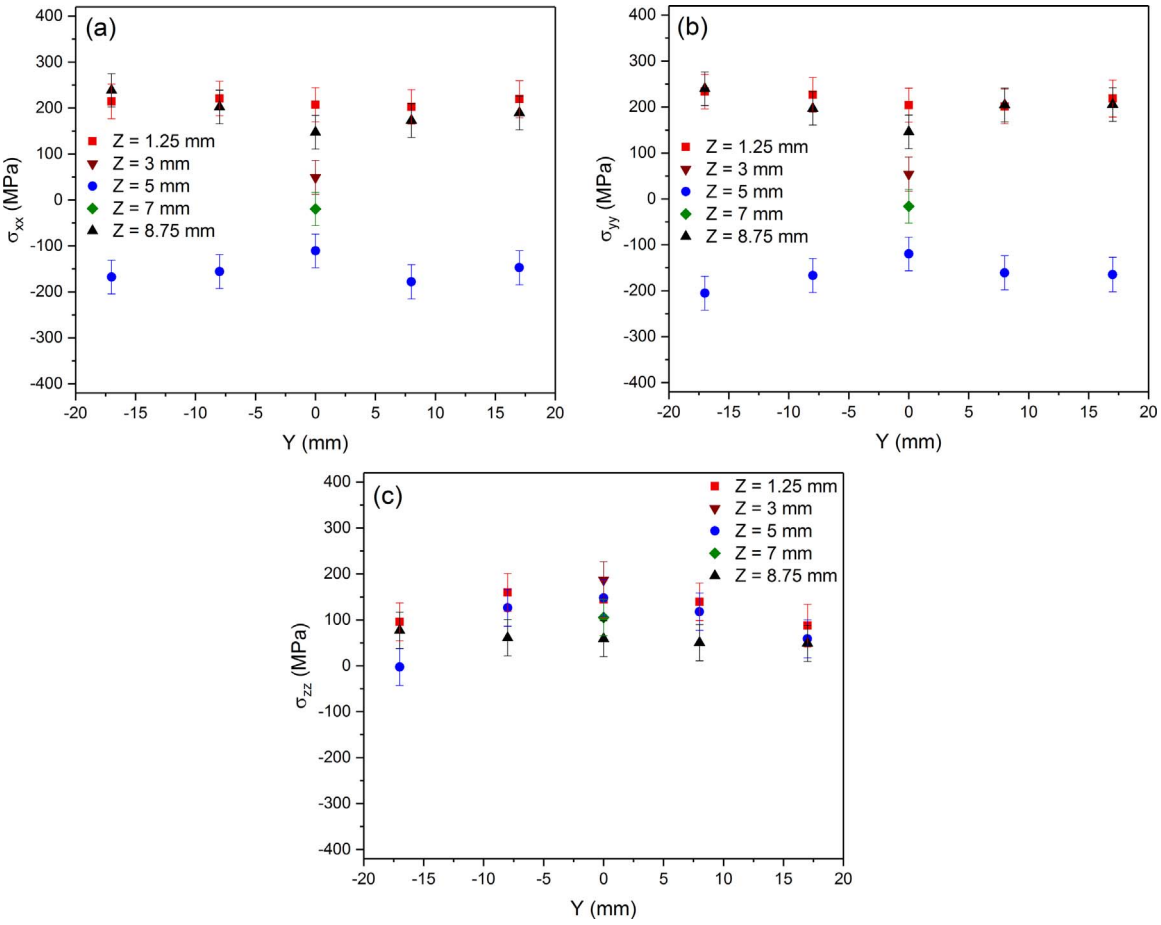


**Fig. 11.** X, Y, and Z components of stress as a function of position along y direction in a disk with diameter and height of 45 mm and 10 mm, respectively after removal from the build plate and support structures.

**Table 4**
Residual stress data for a disk with diameter and height of 45 mm and 10 mm, respectively after removal of the support structures and build plate.

| X (mm) | Y (mm) | Z (mm) | $\sigma_{xx}$ (MPa) | $\sigma_{yy}$ (MPa) | $\sigma_{zz}$ (MPa) |
|---|---|---|---|---|---|
| 0 | −17 | 1.25 | 214.62 | 233.49 | 95.68 |
| 0 | −8 | 1.25 | 221.31 | 226.58 | 159.57 |
| 0 | 0 | 1.25 | 207.19 | 203.99 | 144.65 |
| 0 | 8 | 1.25 | 202.48 | 201.06 | 139.18 |
| 0 | 17 | 1.25 | 219.58 | 218.51 | 87.39 |
| 0 | −17 | 5 | −167.54 | −205.15 | −2.78 |
| 0 | −8 | 5 | −155.71 | −166.73 | 126.24 |
| 0 | 0 | 5 | −110.62 | −119.80 | 147.72 |
| 0 | 8 | 5 | −178.12 | −160.79 | 117.74 |
| 0 | 17 | 5 | −147.32 | −164.61 | 58.76 |
| 0 | −17 | 8.75 | 238.70 | 239.93 | 77.11 |
| 0 | −8 | 8.75 | 202.59 | 196.94 | 61.07 |
| 0 | 0 | 8.75 | 147.43 | 145.84 | 58.90 |
| 0 | 8 | 8.75 | 172.90 | 204.43 | 50.17 |
| 0 | 17 | 8.75 | 189.66 | 205.46 | 48.89 |
| 0 | 0 | 3 | 49.16 | 53.96 | 186.78 |
| 0 | 0 | 7 | −19.33 | −16.02 | 104.86 |

welding [44]; in the latter, heating the part edges during the process can stabilize the stress gradient and consequently mitigate the distortion. The experimental samples in this contribution distorted after removal of the build plate and support structures. In particular, part edges bent up with exhibiting spherical deflection similar to that observed for the additively manufactured components with Charpy test specimen [11], wall [22,25,29] and prism [33] geometries. The distortion level decreased when part became taller and larger in diameter, as shown in Fig. 12. This can be understood given the residual stress profiles for the parts, where the in-plane stress gradient became less steep as part diameter and height increased.

### 4.3. Stress-free locations

Before removal of the build plate and support structures, the magnitude of the in-plane tensile stresses in all disks was significantly greater than that of the compressive ones. In the case of 5 mm height disks, the neutral manifold seemed to be present below the disk mid-height as a consequence of constrain from the build plate and support structures. From in-plane stress distribution of the 10 mm and 15 mm height disks, two neutral manifolds seemed to be present in each disk, one above and the other below the mid-height. To determine the stress-free locations, the in-plane stress as a function of position along the disk height (Z) was plotted separately for all the disks. Then, the plots were fitted by a single line for the 5 mm height disks and two different lines in the case of 10 mm and 15 mm height samples. The x-intercepts of the lines were taken as the heights at which the in-plane stresses were zero. The zero-stress locations for the as-built disks with different dimensions are depicted in Fig. 13. For 5 mm height disks (Fig. 13(a)), most stress-free points (except for the disk edges) were located below the disk mid-height, where the distance from the mid-height increased as the disks became larger in diameter. Near the disk edges, however, the stress-free points were slightly above the disk mid-height. The change in the location of the stress-free points is a consequence of the observed in-plane stress gradient from the disk center to the edges. In the case of 10 mm and 15 mm height disks, two series of stress-free points were determined. The location of these points were shifted further away from

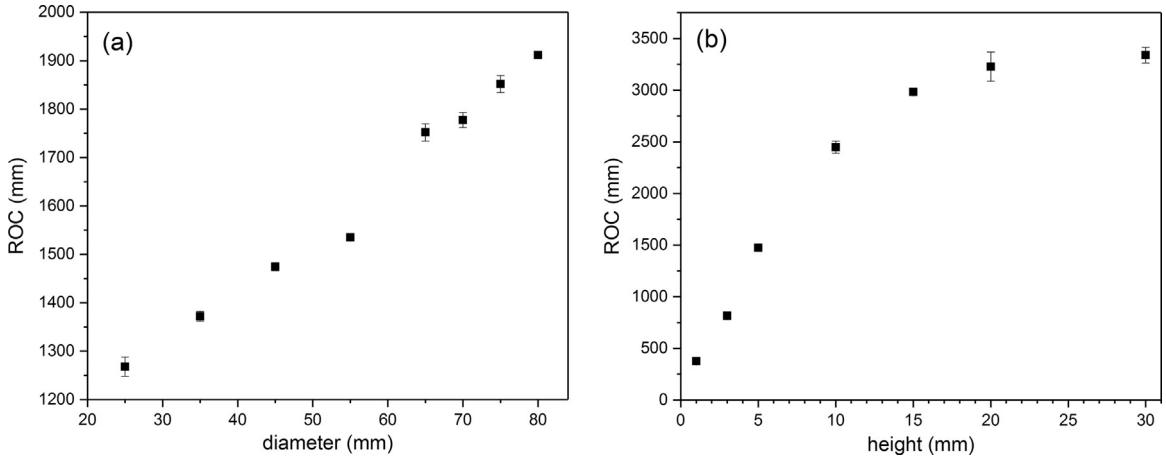


**Fig. 12.** ROC values for the experimental disks after parting from the base plate and support structures; (a) 5 mm height disks with different diameters, (b) 45 mm diameter disks with various heights.

the mid-height when the disks became taller because the magnitude of the tensile residual stresses near the top and bottom surfaces of the disk increased.

## 5. Conclusions

Residual stresses and distortion in the DMLS fabricated disk-shaped 316 L stainless steel components were experimentally measured via neutron diffraction and CMM, respectively. When the disks were attached to the support structures and build plate, the maximum stress magnitude was observed in the longitudinal and transverse directions and was roughly 400 MPa (close to the material yield stress). The in-plane stresses changed from tension near the disk top surface to compression near the bottom surface for the 5 mm height disks. In the case of 10 mm height disks, however, in-plane residual stresses were found to alter from tension near both the top and bottom surfaces to compression at the sample mid-height. The axial residual stresses were negligible for all as-built disks. The magnitude of the in-plane stresses decreased dramatically (up to ≈ 330 MPa) after removal of the build plate and support structures. The stress relaxation for the 5 mm height

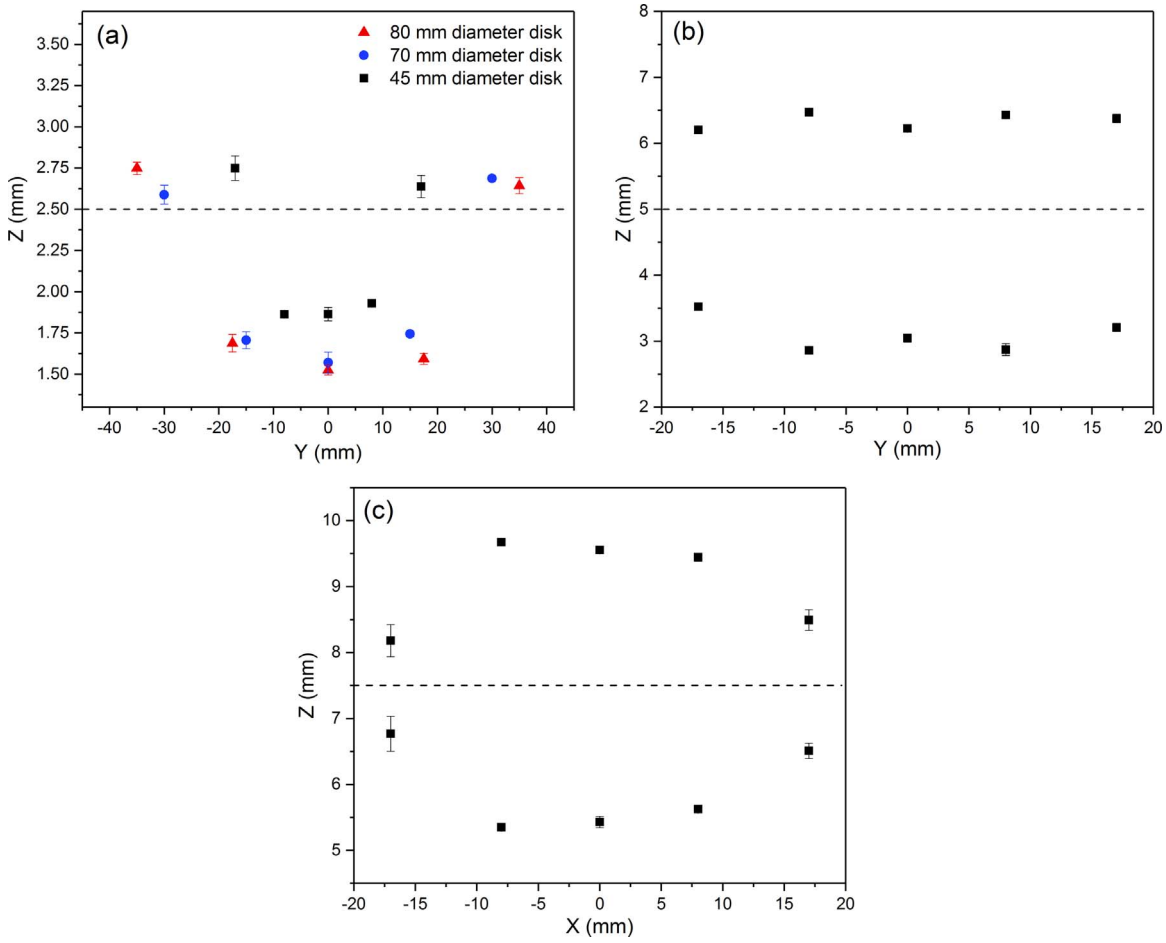


**Fig. 13.** Location of stress-free points within the (a) 5 mm height, (b) 10 mm height, and (c) 15 mm height disks. Dashed lines denote the disk mid-height locations.

disks was more significant than that of 10 mm height ones, leading to a higher distortion level (lower ROC values) for the former. In the case of 5 mm height disks, the stress relaxation increased from the disk edges to the center, where the gradient became steeper for the smaller diameter disks resulting in them displaying higher distortions. The simple geometry employed in this contribution and the achieved data can be used for validation of theoretical models for predicting distortion and residual stresses within DMLS fabricated components.

## Acknowledgements and disclaimer

This effort was performed through the National Center for Defense Manufacturing and Machining under the America Makes Program entitled “Parametric Design of Functional Support Structures for Metal Alloy Feedstocks (Project 4047)” and is based on research sponsored by Air Force Research Laboratory under agreement number FA8650-12-2–7230. The U.S. Government is authorized to reproduce and distribute reprints for Governmental purposes notwithstanding any copyright notation thereon. The views and conclusions contained in this document are those of the authors and should not be interpreted as necessarily representing the official policies, either expressed or implied, of the Government.

Distribution authorized to U.S. Government Agencies and America Makes Members; Critical Technology. Other request for this document shall be referred to AFRL/RXMS, Wright-Patterson Air Force Base, OH 45433-7750.

The authors wish to acknowledge the Canadian Neutron Beam Centre, Canadian Nuclear Laboratories, Chalk River for the neutron beam time.

## References

[1] G.N. Levy, R. Schindel, J.-P. Kruth, Rapid manufacturing and rapid tooling with layer manufacturing (LM) technologies, state of the art and future perspectives, CIRP Ann.-Manuf. Technol. 52 (2003) 589–609.
[2] L.E. Murr, S.M. Gaytan, D.A. Ramirez, E. Martinez, J. Hernandez, K.N. Amato, P.W. Shindo, F.R. Medina, R.B. Wicker, Metal fabrication by additive manufacturing using laser and electron beam melting technologies, J. Mater. Sci. Technol. 28 (2012) 1–14.
[3] X. Wu, A review of laser fabrication of metallic engineering components and of materials, Mater. Sci. Technol. 23 (2007) 631–640.
[4] M.W. Khaing, J.Y.H. Fuh, L. Lu, Direct metal laser sintering for rapid tooling: processing and characterisation of EOS parts, J. Mater. Process. Technol. 113 (2001) 269–272.
[5] A. Simchi, F. Petzoldt, H. Pohl, On the development of direct metal laser sintering for rapid tooling, J. Mater. Process. Technol. 141 (2003) 319–328.
[6] Y. Idell, C. Campbell, L. Levine, F. Zhang, G. Olson, D. Snyder, Characterization of nickel based superalloys processed through direct metal laser sintering technique of additive manufacturing, Microsc. Microanal. 21 (2015) 465–466.
[7] O. Scott-Emuakpor, J. Schwartz, T. George, C. Holycross, C. Cross, J. Slater, Bending fatigue life characterisation of direct metal laser sintering nickel alloy 718, Fatigue Fract. Eng. Mater. Struct. 38 (2015) 1105–1117.
[8] D.H. Smith, J. Bicknell, L. Jorgensen, B.M. Patterson, N.L. Cordes, I. Tsukrov, M. Knezevic, Microstructure and mechanical behavior of direct metal laser sintered Inconel alloy 718, Mater. Charact. 113 (2016) 1–9.
[9] B. AlMangour, J.-M. Yang, Improving the surface quality and mechanical properties by shot-peening of 17-4 stainless steel fabricated by additive manufacturing, Mater. Des. 110 (2016) 914–924.
[10] P.P. Bandyopadhyay, D. Chicot, C.S. Kumar, X. Decoopman, J. Lesage, Influence of sinking-in and piling-up on the mechanical properties determination by indentation: a case study on rolled and DMLS stainless steel, Mater. Sci. Eng.: A 576 (2013) 126–133.
[11] D.W. Brown, J.D. Bernardin, J.S. Carpenter, B. Clausen, D. Spernjak, J.M. Thompson, Neutron diffraction measurements of residual stress in additively manufactured stainless steel, Mater. Sci. Eng.: A 678 (2016) 291–298.
[12] E. Jelis, M. Clemente, S. Kerwien, N.M. Ravindra, M.R. Hespos, Metallurgical and mechanical evaluation of 4340 steel produced by direct metal laser sintering, JOM 67 (2015) 582–589.
[13] J.J. de Damborenea, M.A. Larosa, M.A. Arenas, J.M. Hernández-López, A.L. Jardini, M.C.F. Ierardi, C.A. Zavaglia, R. Maciel Filho, A. Conde, Functionalization of Ti6Al4V scaffolds produced by direct metal laser for biomedical applications, Mater. Des. 83 (2015) 6–13.
[14] P. Promoppatum, R. Onler, S.-C. Yao, Numerical and experimental investigations of micro and macro characteristics of direct metal laser sintered Ti-6Al-4V products, J. Mater. Process. Technol. 240 (2017) 262–273.
[15] G.-L. Huang, S.-G. Zhou, T.-H. Chio, T.-S. Yeo, Fabrication of a high-efficiency waveguide antenna array via direct metal laser sintering, IEEE Antennas Wirel. Propag. Lett. 15 (2016) 622–625.
[16] D. Manfredi, F. Calignano, M. Krishnan, R. Canali, E.P. Ambrosio, E. Atzeni, From powders to dense metal parts: characterization of a commercial AlSiMg alloy processed through direct metal laser sintering, Materials 6 (2013) 856–869.
[17] P. Mercelis, J.-P. Kruth, Residual stresses in selective laser sintering and selective laser melting, Rapid Prototyp. J. 12 (2006) 254–265.
[18] C.A. Brice, W.H. Hofmeister, Determination of bulk residual stresses in electron beam additive-manufactured aluminum, Metall. Mater. Trans. A 44 (2013) 5147–5153.
[19] J. Cao, M.A. Gharghouri, P. Nash, Finite-element analysis and experimental validation of thermal residual stress and distortion in electron beam additive manufactured Ti-6Al-4V build plates, J. Mater. Process. Technol. 237 (2016) 409–419.
[20] R. Cottam, J. Wang, V. Luzin, Characterization of microstructure and residual stress in a 3D H13 tool steel component produced by additive manufacturing, J. Mater. Res. 29 (2014) 1978–1986.
[21] E.R. Denlinger, J.C. Heigel, P. Michaleris, Residual stress and distortion modeling of electron beam direct manufacturing Ti-6Al-4V, Proc. Inst. Mech. Eng., Part B: J. Eng. Manuf. 229 (2015) 1803–1813.
[22] E.R. Denlinger, J.C. Heigel, P. Michaleris, T. Palmer, Effect of inter-layer dwell time on distortion and residual stress in additive manufacturing of titanium and nickel alloys, J. Mater. Process. Technol. 215 (2015) 123–131.
[23] Y. Liu, Y. Yang, D. Wang, A study on the residual stress during selective laser melting (SLM) of metallic powder, Int. J. Adv. Manuf. Technol. 87 (2016) 647–656.
[24] F. Martina, M. Roy, P. Colegrove, S. Williams, Residual stress reduction in high pressure interpass rolled wire + arc additive manufacturing Ti–6Al–4V components, in: Proceedings of the 25th International Solid Freeform Fabrication Symp, 2014, pp. 89–94.
[25] F. Martina, M.J. Roy, B.A. Szost, S. Terzi, P.A. Colegrove, S.W. Williams, P.J. Withers, J. Meyer, M. Hofmann, Residual stress of as-deposited and rolled wire + arc additive manufacturing Ti–6Al–4V components, Mater. Sci. Technol. 32 (2016) 1439–1448.
[26] R.J. Moat, A.J. Pinkerton, L. Li, P.J. Withers, M. Preuss, Residual stresses in laser direct metal deposited Waspaloy, Mater. Sci. Eng.: A 528 (2011) 2288–2298.
[27] P. Rangaswamy, M.L. Griffith, M.B. Prime, T. Holden, R. Rogge, J. Edwards, R. Sebring, Residual stresses in LENS® components using neutron diffraction and contour method, Mater. Sci. Eng.: A 399 (2005) 72–83.
[28] L.M. Sochalski-Kolbus, E.A. Payzant, P.A. Cornwell, T.R. Watkins, S.S. Babu, R.R. Dehoff, M. Lorenz, O. Ovchinnikova, C. Duty, Comparison of residual stresses in Inconel 718 simple parts made by electron beam melting and direct laser metal sintering, Metall. Mater. Trans. A 46 (2015) 1419–1432.
[29] B.A. Szost, S. Terzi, F. Martina, D. Boisselier, A. Prytuliak, T. Pirling, M. Hofmann, D.J. Jarvis, A comparative study of additive manufacturing techniques: residual stress and microstructural analysis of clad and WAAM printed Ti–6Al–4V components, Mater. Des. 89 (2016) 559–567.
[30] B. Vrancken, V. Cain, R. Knutsen, J. Van Humbeeck, Residual stress via the contour method in compact tension specimens produced via selective laser melting, Scr. Mater. 87 (2014) 29–32.
[31] L. Wang, S.D. Felicelli, P. Pratt, Residual stresses in LENS-deposited AISI 410 stainless steel plates, Mater. Sci. Eng.: A 496 (2008) 234–241.
[32] Z. Wang, E. Denlinger, P. Michaleris, A.D. Stoica, D. Ma, A.M. Beese, Residual stress mapping in Inconel 625 fabricated through additive manufacturing: method for neutron diffraction measurements to validate thermomechanical model predictions, Mater. Des. 113 (2017) 169–177.
[33] A.S. Wu, D.W. Brown, M. Kumar, G.F. Gallegos, W.E. King, An Experimental Investigation into Additive Manufacturing-induced Residual Stresses in 316L Stainless Steel, Metall. Mater. Trans. A 45 (2014) 6260–6270.
[34] I. Yadroitsev, I. Yadroitsava, Evaluation of residual stress in stainless steel 316L and Ti6Al4V samples produced by selective laser melting, Virtual Phys. Prototyp. 10 (2015) 67–76.
[35] A. Standard, E837-99, Standard Test Method for Determining Residual Stresses by the Hole-Drilling Strain-Gage Method, American Society for Testing and Materials, Philadelphia, PA, 1992.
[36] M.B. Prime, Cross-sectional mapping of residual stresses by measuring the surface contour after a cut, J. Eng. Mater. Technol. 123 (2001) 162–168.
[37] M.B. Prime, Residual stress measurement by successive extension of a slot: the crack compliance method, Appl. Mech. Rev. 52 (1999) 75–96.
[38] P. Withers, 10 Use of synchrotron X-ray radiation for stress measurement, Anal. residual Stress Diffr. Using Neutron Synchrotron Radiat. (2003) 170.
[39] I.C. Noyan, J.B. Cohen, Residual Stress: Measurement by Diffraction and Interpretation, Springer, 2013.
[40] M.T. Hutchings, P.J. Withers, T.M. Holden, T. Lorentzen, Introduction to the Characterization of Residual Stress by Neutron Diffraction, CRC press, 2005.
[41] B. Clausen, T. Lorentzen, M.A.M. Bourke, M.R. Daymond, Lattice strain evolution during uniaxial tensile loading of stainless steel, Mater. Sci. Eng.: A 259 (1999) 17–24.
[42] K. Saeidi, X. Gao, F. Lofaj, L. Kvetková, Z.J. Shen, Transformation of austenite to duplex austenite-ferrite assembly in annealed stainless steel 316L consolidated by laser melting, J. Alloy. Compd. 633 (2015) 463–469.
[43] P. Jeanmart, J. Bouvaist, Finite element calculation and measurement of thermal stresses in quenched plates of high–strength 7075 aluminium alloy, Mater. Sci. Technol. 1 (1985) 765–769.
[44] M.V. Deo, P. Michaleris, Mitigation of welding induced buckling distortion using transient thermal tensioning, Sci. Technol. Weld. Join. 8 (2003) 49–54.
[45] K. Antony, S. Kumaraguru, D.G. Meda, The effect of neighbourhood scan path exposures on heat buildup: numerical investigations on the laser energy delivery in selective laser sintering process, Int. J. Rapid Manuf. 4 (2014) 119–139.